nature physics

LETTERS

https://doi.org/10.1038/s41567-020-01141-8

A hydrodynamic instability drives protein droplet formation on microtubules to nucleate branches

Sagar U. Setru[1,6], Bernardo Gouveia[2,6], Raymundo Alfaro-Aco[3], Joshua W. Shaevitz[1,4] ✉, Howard A. Stone[5] ✉ and Sabine Petry[3] ✉

Liquid–liquid phase separation[1,2] occurs not only in bulk liquid, but also on surfaces. In physiology, the nature and function of condensates on cellular structures remain unexplored. Here we study how the condensed protein TPX2 behaves on microtubules to initiate branching microtubule nucleation[3–5], which is critical for spindle assembly in eukaryotic cells[6–10]. Using fluorescence, electron and atomic force microscopies and hydrodynamic theory, we show that TPX2 on a microtubule reorganizes according to the Rayleigh–Plateau instability, like dew droplets patterning a spider web[11,12]. After uniformly coating microtubules, TPX2 forms regularly spaced droplets, from which branches nucleate. Droplet spacing increases with greater TPX2 concentration. A stochastic model shows that droplets make branching nucleation more efficient by confining the space along the microtubule where multiple necessary factors colocalize to nucleate a branch.

Branching microtubule nucleation plays a major role in spindle assembly and chromosome segregation in dividing eukaryotic cells, where it is required to generate microtubules in the spindle for kinetochore fibre tension, spindle bipolarity and cytokinesis[6–10]. Its malfunction has been linked to a worse prognosis in cancer[13,14]. The nucleation of a new microtubule from the side of a preexisting microtubule requires TPX2, the augmin complex and the γ-tubulin ring complex (γ-TuRC)[3]. The first component to bind to the preexisting microtubule is TPX2[4], which forms a liquid-like condensate on the microtubule that recruits tubulin and increases branching nucleation efficiency[5]. Other proteins also form condensed phases when associated with microtubules, such as tau[15,16] and BuGZ[17]. Yet, how these proteins behave on the microtubule surface and how this behaviour translates to biological function remain unexplored. Here, we investigate the dynamics of condensed TPX2 on the microtubule. We find that the hydrodynamic Rayleigh–Plateau instability causes TPX2 to form regularly spaced droplets along the microtubule. Then, microtubule branches nucleate from these droplets.

We first studied the dynamics of TPX2 binding to microtubules in vitro using total internal reflection fluorescence (TIRF) microscopy (Fig. 1a,b and TIRF microscopy sample preparation and imaging). Green fluorescent protein GFP–TPX2 at a concentration of 1 μM formed an initially uniform coating along microtubules within seconds. This coating then broke up into a periodic pattern of droplets over tens of seconds with size 0.5 ± 0.1 μm and spacing 0.6 ± 0.2 μm (mean ± s.d., $N = 35$ microtubules) along the microtubules (Supplementary Video 1 and Extended Data Fig. 1). Similar patterns of condensed protein have also been previously observed on single microtubules for TPX2[5] and microtubule bundles for tau[15], BuGZ[17] and LEM2[18]. We next performed the same experiment at a lower, physiological concentration of TPX2, 0.1 μM (refs. [5,19]). We observed a uniform coating but no visible droplet formation (Extended Data Fig. 2a). In contrast, at higher resolution, electron microscopy (Electron microscopy sample preparation and imaging) revealed that regularly spaced droplets do form at 0.1 μM, with size 0.29 ± 0.03 μm and spacing 0.46 ± 0.11 μm (mean ± s.d., $N = 2$ microtubules) (Fig. 1c). This indicates that these droplets can exist below the diffraction limit of visible light. We then reconstituted branching microtubule nucleation in vitro using purified proteins[20] (Methods) and observed that branches originate from TPX2 droplets colocalized with augmin and γ-TuRC (Fig. 1d and Supplementary Video 2). 75 ± 18% of TPX2 droplets nucleated branches (mean ± s.d., $N = 7$ microtubules, Supplementary Table 1). Droplet formation always happened before the nucleation of a branch, and no branches nucleated from areas that did not have droplets. Finally, in meiotic cytosol (Supplementary Methods), microtubules also nucleate from a TPX2-coated microtubule to form a branched network (Extended Data Fig. 2b and Supplementary Video 3). These results suggest that droplet formation from condensed TPX2 may be important for branching microtubule nucleation.

We wished to study the dynamics of droplet formation of TPX2 alone at higher spatial resolution than available by fluorescence microscopy and with temporal resolution not accessible by electron microscopy. Therefore, we turned to atomic force microscopy (AFM) to measure the topography of the initial coating and subsequent beading up of TPX2 on microtubules (AFM sample preparation and imaging). By scanning the AFM tip over the sample every 4 min, with a resolution of ~8 nm in the sample plane and ~1 nm in height, we measured the height of a bare microtubule on a mica surface to be 25 ± 2 nm (mean ± s.d.) (Fig. 2a −5 min and Fig. 2b black line), consistent with the known diameter of 25 nm (ref. [21]). We then added TPX2 at a concentration of 0.2 μM. After addition of TPX2, the height signal uniformly increased to 41 ± 3 nm (mean ± s.d.) as the condensed protein coated the microtubule (Fig. 2a 0 min and Fig. 2b blue line). The film of TPX2 then proceeded to bead up into a periodic pattern of droplets along the microtubule with spacing 250 ± 35 nm (mean ± s.e.m.) (Fig. 2a 60 min, Fig. 2b red line and Supplementary Video 4). The white carets in the 60 min topography in Fig. 2a mark the droplets. The longer timescale to form droplets and the different spacings between droplets in AFM experiments compared with fluorescence and electron microscopy experiments is due to the different biochemical conditions and components

---

[1] Lewis-Sigler Institute for Integrative Genomics, Princeton University, Princeton, NJ, USA. [2] Department of Chemical and Biological Engineering, Princeton University, Princeton, NJ, USA. [3] Department of Molecular Biology, Princeton University, Princeton, NJ, USA. [4] Department of Physics, Princeton University, Princeton, NJ, USA. [5] Department of Mechanical and Aerospace Engineering, Princeton University, Princeton, NJ, USA. [6] These authors contributed equally: Sagar U. Setru, Bernardo Gouveia. ✉e-mail: shaevitz@princeton.edu; hastone@princeton.edu; spetry@princeton.edu

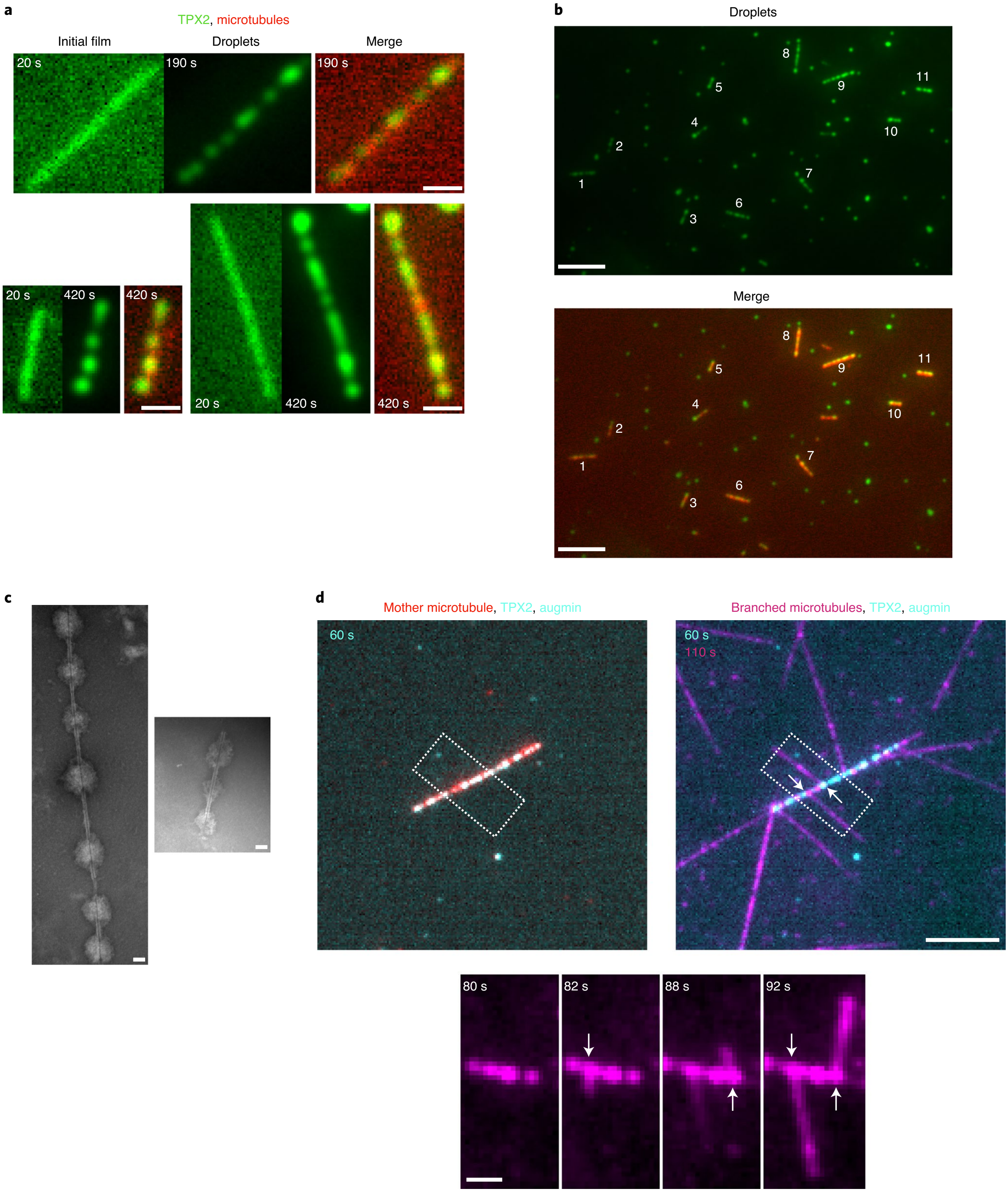

Fig. 1 | TPX2 uniformly coats microtubules and then forms periodically spaced droplets that can nucleate branches. **a**, Initial films and subsequent droplets of TPX2 on microtubules visualized using TIRF microscopy (Supplementary Video 1). GFP–TPX2 at 1 μM was spiked onto a passivated glass surface coated with Alexa568-labelled microtubules. Scale bars, 1 μm. **b**, Large field of view of a TIRF experiment after droplets have formed along microtubules. GFP–TPX2 concentration is 1 μM. Microtubules with a droplet pattern are marked with a number. Scale bars, 5 μm. **c**, TPX2 droplets on microtubules imaged using electron microscopy. GFP–TPX2 at 0.1 μM was incubated with microtubules bound to a carbon grid. Scale bars, 100 nm. **d**, Branched microtubules nucleating from TPX2 droplets formed along the initial mother microtubule, assembled in vitro as in ref. [20] (Supplementary Video 2). Recombinant GFP–augmin and γ-TuRC purified from *X. laevis* meiotic cytosol were included. Arrows indicate branched microtubules. Scale bars, 5 μm (top) and 1 μm (bottom). Only the soluble Cy5–tubulin channel (magenta) was imaged over time to enable a higher frame rate. The GFP–TPX2 and GFP–augmin channel (cyan) and the A568 template microtubule channel (red) were only imaged at the start at 60 s.

used in each experimental method (Supplementary Table 2). The emergent periodicity of the condensate is evident in the power spectrum of the raw height profile along the microtubule averaged over many samples (Fig. 2c). Power spectra rely on the Fourier transform to identify the frequency components of a signal buried in noise (Extended Data Fig. 3 and AFM data analysis). Peaks in a power spectrum indicate the presence of a periodic pattern amidst noise; a monotonic power spectrum is expected for data that lack periodicity. The power spectrum (Fig. 2c) shows no characteristic length scale before and immediately after coating with TPX2, whereas a peak with wavelength 260 ± 20 nm (mean ± s.d.) has emerged by 60 min. Thus, the topography of condensed TPX2 on microtubules exhibits systematic emergent periodicity.

Fluids that coat a solid fibre are known to form droplets via the Rayleigh–Plateau instability[11]. Surface tension causes the film to be unstable due to the curvature of the filament surface, and the surface area is minimized by forming periodically spaced droplets along the fibre[12,22–24]. Following Goren[22], but working directly at low Reynolds number as is appropriate for our experimental system, we solved a linear stability problem for the growth rate σ of the droplet pattern as a function of the wave number $k = 2\pi/\lambda$, where λ is the pattern wavelength (Fig. 3a, Extended Data Fig. 4 and Supplementary Theory). We find that for a given ratio of the microtubule radius to the outer film radius, r_i/r_o, there is a wavelength λ_{max} that grows with the highest growth rate σ_{max} (Fig. 3b). This wavelength will grow exponentially faster than all other wavelengths, leading to a periodic interface with wavelength λ_{max}. Thus, we identify the thicker regions of the AFM height profiles as droplets formed by this instability.

We tested the ability of this theory to explain droplet formation on microtubules by measuring film thicknesses and subsequent droplet spacings at different bulk concentrations of TPX2 (Extended Data Fig. 5). The radius of the microtubule is fixed at $r_i = 25$ nm. However, the thickness of the initial TPX2 film depends on its bulk concentration in solution and the density of microtubules (Extended Data Fig. 6 and Supplementary Theory). Capitalizing on this experimental fact, we changed the initial film thickness from $h = 13 \pm 2$ nm at 0.1 μM TPX2 to $h = 22 \pm 1$ nm at 0.8 μM TPX2 (mean ± s.d.) for a fixed microtubule density. The lower concentrations are physiological in healthy cells[5,19]. The higher concentrations may reflect overexpression in cancer tumour cells, in which TPX2 often has higher genetic copy number[25] and transcript and protein expression[13,26], and can be a negative prognostic indicator[14]. TPX2 formed regularly spaced droplets along microtubules with consistently larger spacings λ_{max} as its bulk concentration increased, following theory (Fig. 3c, Extended Data Fig. 7 and Supplementary Table 3).

Our data exhibit spread for two reasons. First, the dispersion relation we calculate (Fig. 3b) has a broad peak, which means that wavelengths near the maximum growth rate λ_{max} will grow nearly as fast (Fig. 3c, shaded area). Therefore, the discrepancy between the orange curve in Fig. 3c and the measured λ_{max} is a natural consequence of the hydrodynamic theory. Second, low-force (25–40 pN), nanometre-scale AFM in fluid is highly susceptible to thermal noise. This is apparent in the raw height profiles (Extended Data Fig. 3a) and power spectra (Extended Data Fig. 3b) of the microtubule shown in Fig. 2a,b, as well as the power spectra of individual microtubules across the other TPX2 concentrations (Extended Data Fig. 5, right-hand column).

The theory is purely geometric and has no free parameters. The predicted wavelength does not depend on the material properties of the TPX2 condensate such as viscosity or surface tension, which only set the timescale for pattern formation. We note that the higher microtubule density used in AFM experiments (Figs. 2 and 3c) leads to thinner condensed films than in the electron microscopy and reconstitution experiments (Fig. 1) and hence smaller droplet sizes, even at similar TPX2 concentrations (Supplementary Table 2 and Supplementary Theory). In addition, we measured the growth

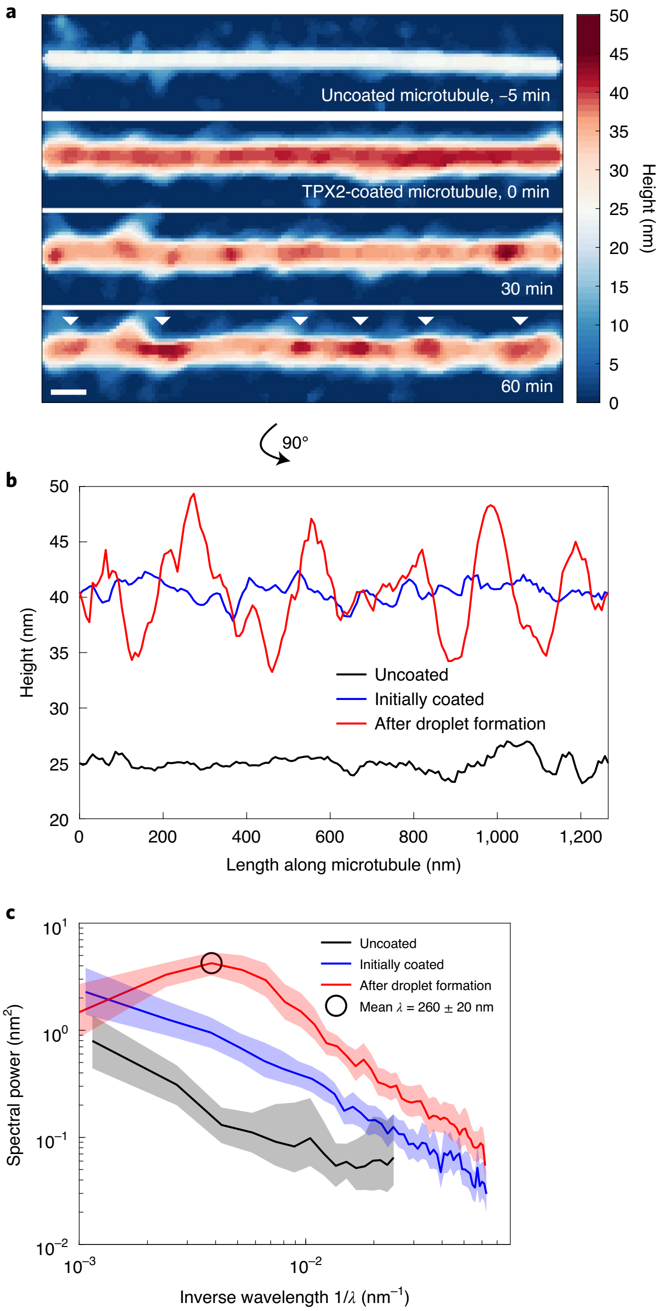

Fig. 2 | AFM measurements reveal condensed TPX2 dynamics on microtubules. a, Time-lapse AFM height topographies of TPX2 uniformly coating and then forming regularly spaced droplets on a microtubule. GFP–TPX2 at 0.2 μM was spiked onto microtubules adhered to a mica surface during data acquisition. This is the entire measured span of the microtubule in the top left of Supplementary Video 4. The topography was smoothed using a 40 nm × 40 nm median filter. White carets mark droplets. Scale bar, 100 nm. **b**, Height profiles centred on the microtubule long axis before coating, just after coating and when droplets have formed on the microtubule surface. Height profiles were smoothed using a moving-average window of 40 nm. The raw height profiles and their power spectra are shown in Extended Data Fig. 3. **c**, Averaged power spectra calculated from the raw height profiles across many microtubules for uncoated ($N = 22$ microtubules), uniformly coated ($N = 23$ microtubules) and droplet-patterned microtubules ($N = 17$ microtubules). A peak is seen only in the data for droplet-patterned microtubules, corresponding to a droplet spacing of 260 ± 20 nm (mean ± s.d.). Shaded regions are 95% bootstrap confidence intervals.

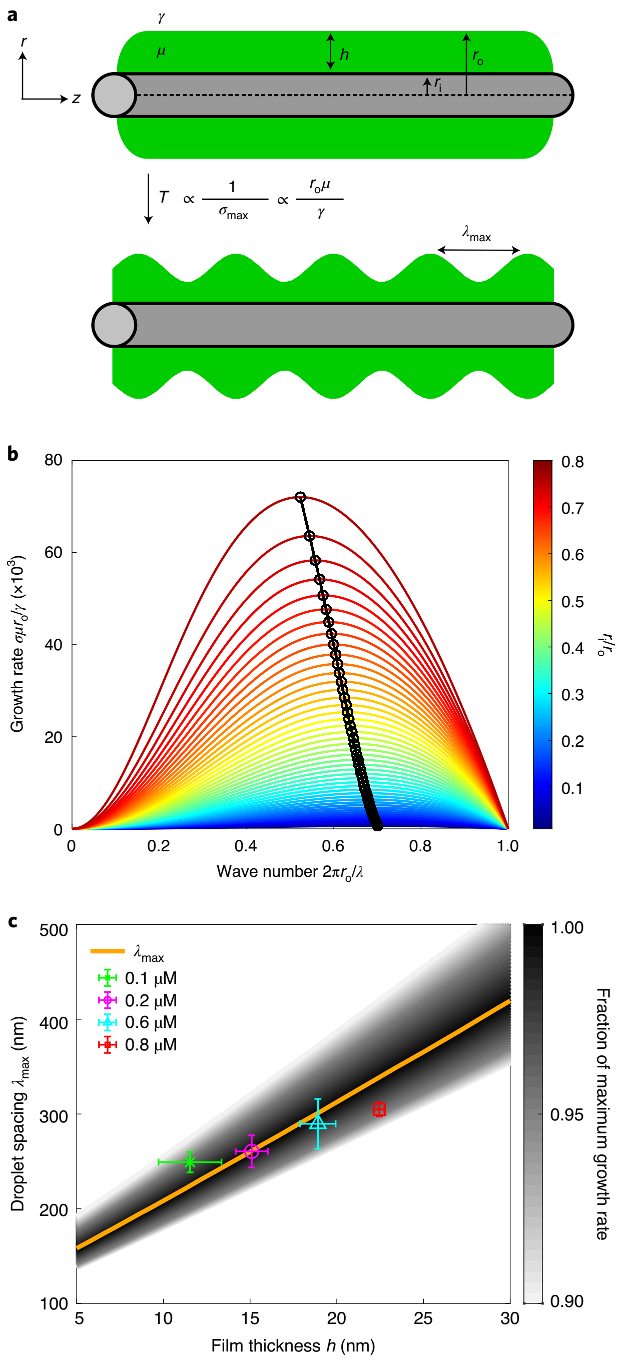

Fig. 3 | Hydrodynamic theory predicts TPX2 droplet formation on a microtubule surface. a, Schematic of the Rayleigh–Plateau instability. TPX2 initially coats the microtubule uniformly with $h = r_o - r_i$. This film breaks up into droplets with spacing λ_{max} due to capillary forces on a timescale $r_o\mu/\gamma$, where μ is the condensate viscosity and γ is the surface tension. **b**, Dispersion relation showing the growth rate versus wave number for different r_i/r_o. The most unstable mode (black circles and line) grows most quickly and corresponds to the observed droplet spacing λ_{max}. **c**, Theoretical prediction for λ_{max} (solid orange line). Overlaid are AFM measurements of the average film thickness and droplet spacing for each TPX2 concentration. The average droplet spacing corresponds to the peak of the averaged power spectra at a given concentration (Extended Data Fig. 7 and Supplementary Table 3). There are no fit parameters. The shaded area encompasses the wavelengths that grow within 10% of the maximum growth rate for each h. In order of increasing concentration, $N = 25$, 17, 23 and 21 microtubules. Error bars are s.d. for h and bootstrapped s.d. for λ_{max}.

rate of λ_{max} to be exponential at early times, as expected for a linear instability (Extended Data Fig. 8). At later times, the periodicity has already been selected as the droplet pattern has set in. Thus, the spectral amplitude versus time stops changing. We also see that the time to form droplets is orders of magnitude longer than the time to grow the initial film. The film grows more quickly because the timescale for its growth is set by fast diffusion of protein in the bulk, whereas the timescale for droplet formation is limited by the slow capillary velocity γ/μ of the condensate (Supplementary Theory). As a control, kinesin-1, a motor protein that does not exist as a condensed phase in any known physiological context and whose binding site on the microtubule is structurally known[27,28], did not exhibit hydrodynamic behaviour on the microtubule as measured by AFM (Extended Data Fig. 7).

How might TPX2 droplets facilitate branching microtubule nucleation? Noting that the process requires the coordinated action in time and space of at least two additional factors, augmin and γ-TuRC, we first imaged the localization of γ-TuRC on microtubules in the presence of TPX2 and augmin using electron microscopy. We found that the ratio of γ-TuRC on microtubules to γ-TuRC on the grid surface was 0.05 ± 0.05 without TPX2 and augmin (mean ± s.d., $N = 3$ microtubules, Extended Data Fig. 9 and Supplementary Table 4). With TPX2 and augmin, this ratio was 0.48 ± 0.04 (mean ± s.d., $N = 4$ microtubules, Supplementary Table 5), confirming that TPX2 and augmin preferentially localize γ-TuRC to microtubules. We observed that multiple γ-TuRCs cluster inside TPX2 droplets spaced 0.25 ± 0.09 μm (mean ± s.d., $N = 4$ microtubules) apart along microtubules (Fig. 4a), consistent with a recent report[20]. The ratio between the number of γ-TuRCs inside TPX2 droplets to the number on bare regions of the same microtubules was 4.8 ± 2.0 (mean ± s.d., $N = 3$ microtubules). Although this is an underestimate, given the difficulty of counting γ-TuRCs in TPX2 droplets, these results demonstrate that γ-TuRC preferentially localizes to TPX2 droplets along microtubules. The first step in branching is the binding of TPX2 to the microtubule, which then localizes the other factors[4]. As such, we hypothesized that regularly spaced TPX2 droplets lead to more efficient colocalization of factors than a uniform coating (Fig. 4b). For a uniform coating, multiple factors must search a greater length along the microtubule before finding each other to nucleate a new branch. With regularly spaced droplets, the explored distance is shorter, which reduces the search time. We performed kinetic Monte Carlo simulations[29] for two factors binding to (with rate k_{on}) and unbinding from (with rate k_{off}) a microtubule of length l with a uniform TPX2 coating and a periodic pattern of TPX2 droplets (Supplementary Theory). These results show that the time τ to colocalize on the microtubule, and hence for nucleation of a new branch, is smaller for droplets than for a uniform layer (Fig. 4c and Extended Data Fig. 10). As a negative control for this model, we used AFM to measure the topography of a carboxy-terminal fragment of TPX2 on microtubules. This fragment is known to be less efficient at nucleating branches in cytosol[5]. Consistent with our model, it did not form droplets on microtubules (Extended Data Fig. 7). Thus, synergistic with TPX2's ability to recruit tubulin[5] and its high concentration as a condensate (Supplementary Theory), its organization into droplets partitions the microtubule so that multiple factors can more easily find each other. Taken together, TPX2's phase behaviour enhances reaction kinetics via droplet patterning, condensate concentration and tubulin recruitment.

It is important to think about our model in a cellular context. During cell division, TPX2 is released as a gradient in the vicinity of chromosomes[30]. The typical TPX2 concentration in *Xenopus laevis* is 90 nM (ref. [19]) and the typical gradient length is ~10 μm (ref. [30]). This gives ~2×10^5 TPX2 molecules that are available to condense on microtubules near chromosomes, assuming a spherical volume. We estimate the concentration of TPX2 in the condensed phase to

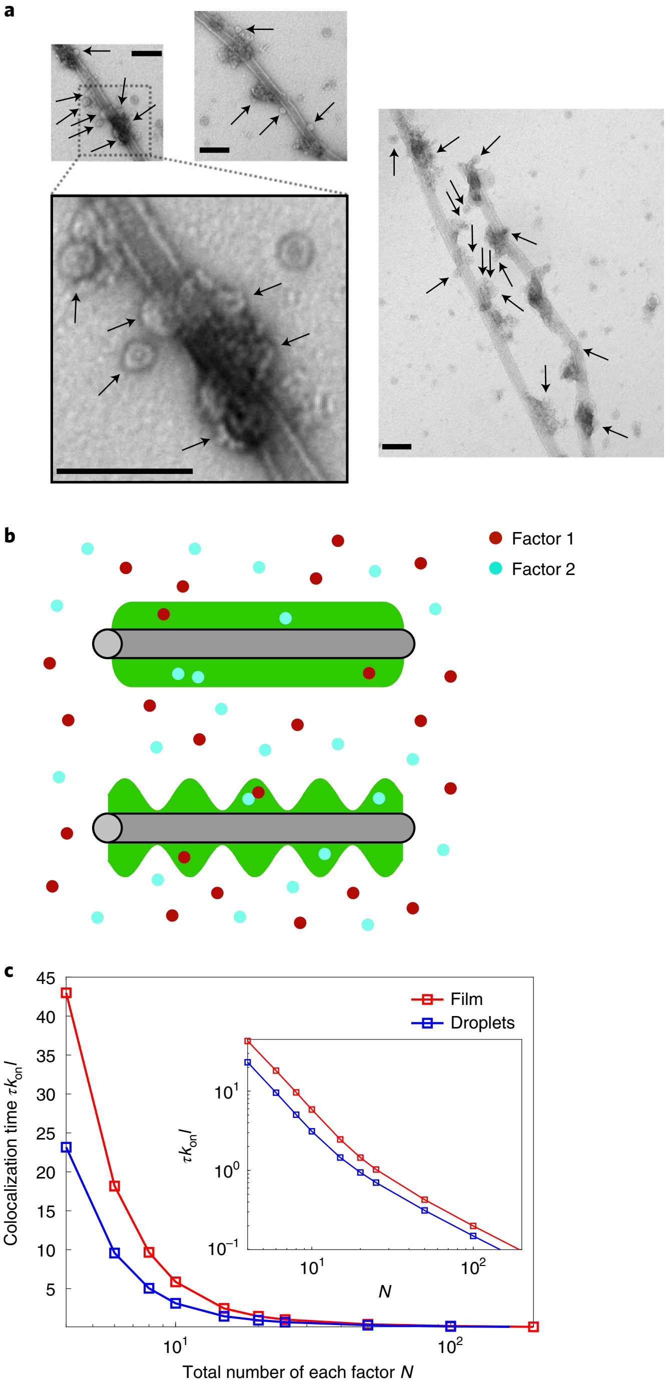

Fig. 4 | A stochastic model predicts that TPX2 droplets enhance the efficiency of branching microtubule nucleation. a, Electron microscopy images show ring-shaped γ-TuRCs (black arrows) localizing to regularly spaced TPX2 droplets along the microtubule in the presence of augmin. Scale bars, 100 nm. **b**, Schematic of branching factors binding to a microtubule coated with a uniform TPX2 layer versus periodic TPX2 droplets. **c**, Monte Carlo simulations show that droplets colocalize two necessary factors faster than a uniform coating. Here, $k_{on}l/k_{off} = 10$. These results are not sensitive to this parameter choice (Extended Data Fig. 10). Each datapoint is the average of 10^7 independent simulations.

be $10^4\,\mu m^{-3}$ using our AFM experiments (Supplementary Methods). There are then ~80 TPX2 molecules needed to form a 10 nm condensed film on a typical 7-µm-long, 25-nm-diameter microtubule[31]. Therefore, TPX2 can coat ~3×10^3 microtubules during cell division. Given that the density of microtubules in the metaphase spindle is ~$2\,\mu m^{-3}$ within 10 µm of chromosomes[31], ~8×10^3 microtubules lie in the vicinity of chromosomes. Thus, TPX2 can coat ~40% of the metaphase microtubule mass near chromosomes at this film thickness. We hypothesize that the Rayleigh–Plateau instability is most relevant during early spindle assembly to accelerate the generation of microtubules, as TPX2 is responsible for creating most of the spindle microtubules via branching nucleation[32], in particular during early stages of spindle assembly[8].

As the study of liquid-like protein condensates has intensified[1,2], the physical phenomenology has been dominated by optical observations of droplets in solution or on microtubules. Here, we quantitatively demonstrate the emergence of non-trivial hydrodynamic features such as films and spatiotemporal periodic instabilities that arise when a condensate interacts with a filament. In future work, it will be interesting to explore how multiple proteins, such as TPX2 and BuGZ[17], condense on the microtubule, as multiprotein condensates in solution have been reported[33]. We suspect that interfacial physics could manifest itself in other ways when condensates interact with cellular filaments, such as via elastocapillary effects[34] that could produce forces between cytoskeletal filaments or other semi-flexible macromolecules such as RNA and DNA[35].

Online content

Any methods, additional references, Nature Research reporting summaries, source data, extended data, supplementary information, acknowledgements, peer review information; details of author contributions and competing interests; and statements of data and code availability are available at https://doi.org/10.1038/s41567-020-01141-8.

Received: 31 January 2020; Accepted: 24 November 2020;

References

1. Shin, Y. & Brangwynne, C. P. Liquid phase condensation in cell physiology and disease. *Science* **357**, eaaf4382 (2017).
2. Alberti, S., Gladfelter, A. & Mittag, T. Considerations and challenges in studying liquid–liquid phase separation and biomolecular condensates. *Cell* **176**, 419–434 (2019).
3. Petry, S., Groen, A., Ishihara, K., Mitchison, T. & Vale, R. Branching microtubule nucleation in *Xenopus* egg extracts mediated by augmin and TPX2. *Cell* **152**, 768–777 (2013).
4. Thawani, A., Stone, H. A., Shaevitz, J. W. & Petry, S. Spatiotemporal organization of branched microtubule networks. *eLife* **8**, e43890 (2019).
5. King, M. R. & Petry, S. Phase separation of TPX2 enhances and spatially coordinates microtubule nucleation. *Nat. Commun.* **11**, 270 (2020).
6. Uehara, R. & Goshima, G. Functional central spindle assembly requires de novo microtubule generation in the interchromosomal region during anaphase. *J. Cell Biol.* **191**, 259–267 (2010).
7. Uehara, R. et al. The augmin complex plays a critical role in spindle microtubule generation for mitotic progression and cytokinesis in human cells. *Proc. Natl Acad. Sci. USA* **106**, 6998–7003 (2009).
8. Petry, S., Pugieux, C., Nédélec, F. J. & Vale, R. D. Augmin promotes meiotic spindle formation and bipolarity in *Xenopus* egg extracts. *Proc. Natl Acad. Sci. USA* **108**, 14473–14478 (2011).
9. Lawo, S. et al. HAUS, the 8-subunit human augmin complex, regulates centrosome and spindle integrity. *Curr. Biol.* **19**, 816–826 (2009).
10. Hotta, T. et al. Characterization of the *Arabidopsis* augmin complex uncovers its critical function in the assembly of the acentrosomal spindle and phragmoplast microtubule arrays. *Plant Cell* **24**, 1494–1509 (2012).
11. Rayleigh, L. On the instability of jets. *Proc. Lond. Math. Soc.* **1**, 4–13 (1878).
12. Quéré, D. Fluid coating on a fiber. *Annu. Rev. Fluid Mech.* **31**, 347–384 (1999).
13. Pérez de Castro, I. & Malumbres, M. Mitotic stress and chromosomal instability in cancer: the case for TPX2. *Genes Cancer* **3**, 721–730 (2012).
14. Uhlen, M. et al. A pathology atlas of the human cancer transcriptome. *Science* **357**, eaan2507 (2017).
15. Hernández-Vega, A. et al. Local nucleation of microtubule bundles through tubulin concentration into a condensed tau phase. *Cell Rep.* **20**, 2304–2312 (2017).

16. Siahaan, V. et al. Kinetically distinct phases of tau on microtubules regulate kinesin motors and severing enzymes. *Nat. Cell Biol.* **21**, 1086–1092 (2019).
17. Jiang, H. et al. Phase transition of spindle-associated protein regulate spindle apparatus assembly. *Cell* **163**, 108–122 (2015).
18. von Appen, A. et al. LEM2 phase separation promotes ESCRT-mediated nuclear envelope reformation. *Nature* **582**, 115–118 (2020).
19. Wühr, M. et al. Deep proteomics of the *Xenopus laevis* egg using an mRNA-derived reference database. *Curr. Biol.* **24**, 1467–1475 (2014).
20. Alfaro-Aco, R., Thawani, A. & Petry, S. Biochemical reconstitution of branching microtubule nucleation. *eLife* **9**, e49797 (2020).
21. Desai, A. & Mitchison, T. J. Microtubule polymerization dynamics. *Annu. Rev. Cell Dev. Biol.* **13**, 83–117 (1997).
22. Goren, S. L. The instability of an annular thread of fluid. *J. Fluid Mech.* **12**, 309–319 (1962).
23. Boulogne, F., Pauchard, L. & Giorgiutti-Dauphiné, F. Instability and morphology of polymer solutions coating a fibre. *J. Fluid Mech.* **704**, 232–250 (2012).
24. Haefner, S. et al. Influence of slip on the Plateau–Rayleigh instability on a fibre. *Nat. Commun.* **6**, 4–9 (2015).
25. Tonon, G. et al. High-resolution genomic profiles of human lung cancer. *Proc. Natl Acad. Sci. USA* **102**, 9625–9630 (2005).
26. Neumayer, G., Belzil, C., Gruss, O. J. & Nguyen, M. D. TPX2: of spindle assembly, DNA damage response, and cancer. *Cell. Mol. Life Sci.* **71**, 3027–3047 (2014).
27. Cao, L. et al. The structure of apo-kinesin bound to tubulin links the nucleotide cycle to movement. *Nat. Commun.* **5**, 5364 (2014).
28. Shang, Z. et al. High-resolution structures of kinesin on microtubules provide a basis for nucleotide-gated force-generation. *eLife* **3**, e04686 (2014).
29. Gillespie, D. T. Exact stochastic simulation of coupled chemical reactions. *J. Phys. Chem.* **81**, 2340–2361 (1977).
30. Caudron, M., Bunt, G., Bastiaens, P. & Karsenti, E. Spatial coordination of spindle assembly by chromosome-mediated signaling gradients. *Science* **309**, 1373–1376 (2005).
31. Brugués, J., Nuzzo, V., Mazur, E. & Needleman, D. J. Nucleation and transport organize microtubules in metaphase spindles. *Cell* **149**, 554–564 (2012).
32. Decker, F., Oriola, D., Dalton, B. & Brugués, J. Autocatalytic microtubule nucleation determines the size and mass of *Xenopus laevis* egg extract spindles. *eLife* **7**, e31149 (2018).
33. Feric, M. et al. Coexisting liquid phases underlie nucleolar subcompartments. *Cell* **165**, 1686–1697 (2016).
34. Duprat, C., Protiere, S., Beebe, A. & Stone, H. A. Wetting of flexible fibre arrays. *Nature* **482**, 510–513 (2012).
35. Li, Q. et al. LLPSDB: a database of proteins undergoing liquid–liquid phase separation in vitro. *Nucleic Acids Res.* **48**, D320–D327 (2020).

Methods

Protein expression and purification. Recombinant GFP–TPX2 was purified as previously described[4,36]. Full-length TPX2 or C-terminal TPX2 (amino acids 377 to 716) tagged on the amino terminus with Strep–6×His–GFP–TEV was cloned into the pST50 expression vector. TPX2 was expressed in *Escherichia coli* (strain Rosetta 2) for 7 h at 25 °C and the cells lysed using an EmulsiFlex (Avestin) in lysis buffer (50 mM Tris-HCl at pH 8.0, 150 mM imidazole, 750 mM NaCl, 2.5 mM phenylmethyl sulfonyl fluoride (PMSF), 6 mM β-mercaptoethanol (BME), one cOmplete EDTA-free protease inhibitor tablet (Sigma) and 1,000 U DNase I (Sigma)). Then, the protein was affinity purified using Ni-NTA (nitrilotriacetic acid) beads in binding buffer (50 mM Tris-HCl at pH 8.0, 750 mM NaCl, 15 mM imidazole, 2.5 mM PMSF, 6 mM BME). Next, the protein was eluted with 200 mM imidazole, and the protein was pooled and diluted fourfold to a final NaCl concentration of 200 mM. Afterwards, nucleotides were removed from the eluted protein with a HiTrap heparin HP column (GE Healthcare). Protein was bound to the column in 250 mM NaCl and then isocratic elution was carried out in 750 mM NaCl. Solutions were prepared in heparin buffer (50 mM Tris-HCl at pH 8.0, 2.5 mM PMSF, 6 mM BME). Finally, peak fractions were pooled and loaded onto a Superdex 200 pg 16/600 gel filtration column. Gel filtration was performed in CSF-XB buffer (10 mM K-HEPES at pH 7.7, 100 mM KCl, 1 mM $MgCl_2$, 5 mM EGTA) with 10% (w/v) sucrose. TPX2 was flash frozen in liquid nitrogen and stored at −80 °C until use. This TPX2 was used for all fluorescence, electron and atomic force microscopy experiments.

Recombinant GFP-tagged augmin holocomplex was purified as previously described[20,37]. Briefly, Sf9 cells were coinfected with several baculoviruses, each carrying a subunit of the augmin complex, at multiplicity of infection values of 1–3. Cells were collected and lysed 72 h after infection. Augmin subunit HAUS6 had an N-terminal ZZ-tag, subunit HAUS2 had a C-terminal GFP–6×His and the other six subunits were untagged. The complex was affinity purified using IgG–Sepharose (GE Healthcare) and eluted via cleavage with 100–200 μg of glutathione *S*-transferase (GST)–HRV3C protease. The HRV3C protease was subsequently removed using a GSTrap 5 ml column (GE Healthcare). The sample was further purified and concentrated using Ni-NTA agarose beads. The protein complex was dialysed overnight into CSF-XB with 10% (w/v) sucrose. Augmin was flash frozen in liquid nitrogen and stored at −80 °C until use.

γ-TuRC was purified from *X. laevis* meiotic cytoplasm as done previously[20]. First, 5–10 ml of cytoplasm was prepared from *X. laevis* eggs using standard procedures[38,39] and diluted 10-fold in CSF-XB with 10% sucrose (w/v), 10 μg each of leupeptin, pepstatin and chymostatin, 1 mM GTP and 1 mM dithiothreitol (DTT). The larger particles in the cytosol were removed by low-speed centrifugation at 3,000 *g* for 10 min at 4 °C. The supernatant was diluted twofold with buffer and passed through 1.2 μm, 0.8 μm and 0.22 μm pore size filters. γ-TuRC was precipitated by adding a solution of 6.5% (w/v) polyethylene glycol (PEG) 8,000 to the filtrate on ice for 30 min. After centrifuging at 17,000 *g* for 20 min at 4 °C, the pellet was resuspended in 15 ml of CSF-XB with 10% sucrose (w/v), 10 μg each of leupeptin, pepstatin and chymostatin, 1 mM GTP, 1 mM DTT and 0.05% (v/v) NP-40 detergent. The resuspension was centrifuged at 136,000 *g* for 7 min at 4 °C. Then, protein A Sepharose beads (GE Healthcare) were used to preclear the supernatant for 20 min at 4 °C. The beads were removed via centrifugation. Then 2–4 ml of γ-tubulin antibody (Sigma) at 1 mg ml^{-1} was added and the mixture was rotated for 2 h at 4 °C. After this, 1 ml of washed protein A Sepharose beads was incubated with the sample on a rotator for 2 h at 4 °C. The beads were collected by spinning and then transferred to a column with CSF-XB with 10% sucrose (w/v), 10 μg each of leupeptin, pepstatin and chymostatin, 1 mM GTP, 1 mM DTT and 0.05% (v/v) NP-40 detergent. The beads were washed with CSF-XB with 10% sucrose (w/v), 10 μg each of leupeptin, pepstatin and chymostatin, 1 mM GTP, 1 mM DTT and 150 mM additional KCl, then with CSF-XB with 1 mM ATP, and finally with CSF-XB to remove the ATP. For biotinylation of γ-TuRC, done to visualize the reconstitution using fluorescence microscopy, 25 μM of *N*-hydroxysuccinimide (NHS)–PEG4–biotin (Thermo Scientific) was incubated with the beads in CSF-XB for 1 h at 4 °C, and unreacted reagent was washed away with CSF-XB before elution. To elute γ-TuRC from the beads, 2 ml of a γ-tubulin peptide (amino acids 412–451) at 0.5 mg ml^{-1} in CSF-XB was added to the column and incubated overnight. The eluted sample was collected from the column the following day. γ-TuRC was then concentrated using a 100 kDa centrifuge filter (Amicon). This concentrated sample was loaded onto a 10–50% (w/w) continuous sucrose gradient in CSF-XB buffer with 10 μg each of leupeptin, pepstatin and chymostatin, 1 mM GTP and 1 mM DTT. The gradient was centrifuged for 3 h at 4 °C at 200,000 *g* in a TLS55 rotor (Beckman). Fractions of the sucrose gradient were collected manually from the top of the gradient. The fractions with the highest γ-tubulin signal as determined by western blot were combined and concentrated as above using a 100 kDa centrifuge filter. Purified γ-TuRC was used within two days without freezing and kept on ice.

The kinesin-1 fragment K560–GFP was purified as previously described[40]. Amino acids 1–560 of human conventional kinesin tagged on the C terminus with GFP and 6×His were cloned into pET17B vector[40]. K560–GFP was expressed in *E. coli* for 4 h at 37 °C and the cells lysed as above using lysis buffer (50 mM $NaPO_4$ at pH 8.0, 250 mM NaCl, 1 mM $MgCl_2$, 20 mM imidazole, 10 mM BME, 0.5 mM PMSF, 0.5 mM ATP, one cOmplete EDTA-free protease inhibitor tablet, 1,000 U DNase I). Then, K560-GFP was affinity purified using a HisTrap HP column (GE Healthcare) using binding buffer (50 mM $NaPO_4$ at pH 8.0, 250 mM NaCl, 1 mM $MgCl_2$, 20 mM imidazole, 10 mM BME, 0.5 mM PMSF, 0.5 mM ATP) and eluted using binding buffer at 500 mM imidazole. Peak fractions were pooled and dialysed overnight at 4 °C into CSF-XB buffer.

Bovine brain tubulin was labelled with Cy5 or Alexa568 NHS ester (GE Healthcare) or biotin–PEG4–NHS (Thermo Scientific) using methods previously described[41].

Protein concentrations were determined by SDS–PAGE and then Coomassie staining of a concentration series of the protein of interest alongside a BSA standard, or using Bradford dye (Bio-Rad).

Polymerization of GMPCPP-stabilized microtubules. For TIRF microscopy experiments, double-cycled guanosine-5′-[(α,β)-methyleno]triphosphate (GMPCPP)-stabilized microtubules were prepared[41]. Bovine tubulin at 20 μM was polymerized in BRB80 (80 mM K-PIPES at pH 6.8, 1 mM EGTA, 1 mM $MgCl_2$), with 10 mM GMPCPP (Jena Bioscience), 2 mM Alexa568-labelled tubulin and 2 mM biotin-labelled tubulin, at 37 °C for 30 min. Microtubules were pelleted via centrifugation at 126,000 *g* for 8 min, and depolymerized by resuspending and incubating in ice-cold BRB80 totalling 80% of the original volume for 20 min. GMPCPP was then added to 10 mM, and microtubules were again polymerized and pelleted as in the first cycle. Microtubules were flash frozen in liquid nitrogen and quickly thawed before use. Microtubules were used at a final 1,000-fold to 2,000-fold dilution for TIRF experiments.

For electron and atomic force microscopy, bovine tubulin at 20 μM was incubated in BRB80 with 10 mM GMPCPP (Jena Bioscience) on ice for 5 min and then centrifuged at 90,000 r.p.m. in a TLA100 rotor (Beckman) at 4 °C for 15 min. The supernatant was then incubated at 37 °C for 30 to 60 min to polymerize the microtubules. Finally, the reaction mixture was diluted fivefold and microtubules were pelleted via centrifugation as above at 27 °C for 5 min. The supernatant was discarded and microtubules resuspended in the original volume of BRB80. Microtubules were made fresh for each imaging day and diluted 500-fold for electron microscopy and 10-fold for AFM.

Reconstitution of microtubule branching nucleation in vitro. Branching microtubule nucleation was reconstituted in vitro using purified proteins as was done recently[20]. Briefly, microtubules were attached to a flow chamber made with PEG-passivated and biotinylated glass coverslips. A mixture of TPX2 (0.05 μM), augmin (0.05 μM) and γ-TuRC was incubated on ice for 5 min and then passed into the chamber. Proteins were allowed to bind microtubules and excess protein was passed out. Then, BRB80 with 30 mM KCl, 1 mM GTP, 5 mM BME, 0.075% (w/v) methylcellulose (4,000 cP), 1% (w/v) glucose, 0.02% (v/v) Brij-35, 250 nM glucose oxidase, 64 nM catalase, 1 mg ml^{-1} BSA, 19 μM unlabelled bovine tubulin and 1 μM Cy5-labelled bovine tubulin was passed into the chamber to initiate the nucleation and growth of branched microtubules via TIRF microscopy.

TIRF microscopy sample preparation and imaging. Coverslip-bottomed culture well plates (Grace Bio-Labs) were functionalized with anti-biotin antibody (Abcam) at 0.1 mg ml^{-1} concentration at room temperature for 10 min. Excess antibody was washed out by serially diluting in buffer (CSF-XB at 50–60 mM KCl or BRB80) three times, and then the coverslip blocked with κ-casein at 1 mg ml^{-1}. Excess κ-casein was washed out by serially diluting in buffer as above. Then, microtubules were allowed to settle and bind the coverslip surface for 10 min at room temperature and unbound microtubules were removed via serial dilution as above. TPX2 was then pipetted into the wells during image acquisition, to visualize TPX2 coating and forming droplets on microtubules.

TIRF microscopy was done using a Nikon Ti-E microscope with a 100× magnification, 1.49 numerical aperture objective. An Andor Zyla scientific complementary metal–oxide–semiconductor camera was used for acquisition. Images were acquired using NIS-Elements software (Nikon). For imaging of the reconstitution of branching microtubule nucleation, the objective was heated to 33 °C using an objective heater (Bioptechs).

TIRF data analysis. Droplet sizes and spacings used to create Extended Data Fig. 1a were calculated manually using Fiji (ImageJ)[42]. To calculate the average power spectrum in Extended Data Fig. 1b, line scans of droplet-patterned microtubules in the raw TIRF images were taken in Fiji and Fourier transformed in MATLAB. The power spectrum is given by the formula

$$P(f) = |\hat{I}(f)|^2 = \left|\frac{1}{L}\int_0^L I(z)\,\mathrm{e}^{-2\pi i f z}\,\mathrm{d}z\right|^2 \qquad (1)$$

where I is the intensity, z is the position along the microtubule, L is the length of the microtubule and f is a spatial frequency. This is analogous to equation (2) used for the AFM data and described in AFM data analysis. These power spectra were then averaged. The frequency at which the average power spectrum is maximal corresponds to the average observed droplet spacing, as is also the case for the AFM data (AFM data analysis).

Electron microscopy sample preparation and imaging. For experiments with TPX2 alone, microtubules were incubated for 5 min at room temperature on plasma-treated carbon grids (Electron Microscopy Sciences). Excess microtubules were wicked away, and then TPX2 diluted in BRB80 was pipetted onto the grids. TPX2 was incubated with microtubules on the grids for 1 h to let droplets form, and kept in a humidity chamber to prevent evaporation.

For experiments to see colocalization of γ-TuRC with TPX2 droplets, microtubules were first incubated with a mixture of 50 nM TPX2, 50 nM augmin and γ-TuRC. The sample was diluted 10-fold with BRB80 and 5 µL of the diluted sample was immediately applied to plasma-treated carbon grids. Then, for both experiments, all liquid was wicked away and samples were stained by blotting the grids three times with 2% uranyl acetate, after which the grids were left to dry. Images were collected with a CM100 transmission electron microscope (Philips) operated at 80 keV with 64,000× magnification and recorded using an ORCA camera.

AFM sample preparation and imaging. Microtubules were bound to mica discs using divalent cations, as previously described[43]. Mica discs were mounted on metal discs using double-sided sticky tape (supplies all from Ted Pella). A fresh mica layer was exposed by peeling off the previous layer using tape, and 1 M $MgCl_2$ was pipetted onto the mica disc and incubated at room temperature for 10 min. $MgCl_2$ was blown off using nitrogen gas and microtubules were immediately deposited onto the mica disc and allowed to bind for 10 min. Unbound microtubules were washed off using BRB80. The mica disc was mounted on the AFM stage using a magnet.

AFM was carried out using a Bruker BioScope Resolve operated in peak-force fluid tapping mode using PEAKFORCE-HIRS-F-A or B probes (Bruker), with peak force set to 25–40 pN. These probes have a nominal tip radius of 1 nm and a stiffness of $0.35\,\mathrm{N\,m^{-1}}$ or $0.12\,\mathrm{N\,m^{-1}}$, respectively. A 1 Hz scan rate per pixel row was used to sample a 2 µm × 2 µm area every ~4.25 min. Resulting topographies were 256 × 256 pixels, yielding a lateral pixel size of about 8 nm. After uncoated microtubules were imaged, TPX2 or kinesin-1 was gently pipetted into the fluid meniscus above the mica disc and below the AFM scan head so that protein could bind microtubules while the AFM was scanning the sample. Care was taken to insure that the volume of the meniscus varied minimally between experiments; note that the volume of the meniscus will affect the bulk TPX2 concentration. The AFM continued scanning the sample for 40 to 180 min as TPX2 droplets formed. We waited a similar amount of time to probe kinesin-bound microtubules. For most experiments, once TPX2 droplets had formed, after about 40 min, we moved the stage to a different area of the sample to collect more data from microtubules that were not probed as the droplets formed. This confirms that the act of poking TPX2-coated microtubules repetitively with the AFM probe does not generate the patterns. For these microtubules, for which the initial film thickness was not measured, the film thickness used for Fig. 3c was the average of all film thicknesses measured in that sample, which was always within ~1–2 nm. For the highest TPX2 concentration range tested, $0.8 \pm 0.4\mu$M, larger topographies (4 µm × 4 µm, sampled 512 × 512 at a 0.5 Hz scan rate per pixel row so that the speed of the AFM probe was the same across the sample as in the smaller images) were taken once the patterns formed to enable sampling of larger distances between droplets.

AFM data analysis. Raw AFM topographies were processed using Gwyddion data visualization and analysis software[44] to remove horizontal scarring and linear and polynomial background, and to align rows along the scan axis. Topographical line scans along bare, uncoated microtubules and along microtubules within one frame (~4 min) of the initial TPX2 coating were drawn to determine the film thickness. Successive topographies of the same area were registered in Fiji (ImageJ)[42] using the StackReg and TurboReg packages[45]. To systematically measure the spacing between TPX2 droplets, power spectra of line scans along TPX2-droplet-coated microtubules were calculated using MATLAB. Power spectra use the Fourier transform to decompose a line scan into a spectrum of the strength of all spatial frequencies in the original line scan. Analogously to equation (1), power spectra were calculated by squaring the absolute value of the normalized finite Fourier transform $\hat{h}(f)$ of the height profiles $h(z)$:

$$P(f) = |\hat{h}(f)|^2 = \left|\frac{1}{L}\int_0^L h(z)\,\mathrm{e}^{-2\pi i f z}\,\mathrm{d}z\right|^2 \qquad (2)$$

L is the length of the height profile. For each microtubule, multiple (at least three) spectra were collected, and then an average spectrum for each TPX2 concentration was determined via bootstrapping over the distribution of individual spectra.

The inverse of the frequency at which the peak power in the average spectrum occurs corresponds to the spacing between TPX2 droplets: $\lambda = 1/f$, as is also the case for the fluorescence data (TIRF data analysis). Due to the noise in the AFM data, the sizes of the droplets were not measured, as they were manually measured for electron microscopy and TIRF microscopy data. Furthermore, the noise in the AFM data also meant that the peaks in individual spectra were not reliable, which is why we averaged the individual spectra. Microtubules that broke apart or were too short to sample low spatial frequencies, and sections of microtubules that curved or were under crisscrossing microtubules, were excluded from analysis. Some line scans were high-pass filtered via a large smoothing window (~300–400 nm) when they still exhibited local linear or polynomial background. Line scans were never low-pass filtered to determine spectra. To verify that the growth rate of the droplets was exponential in time, as predicted by theory, the power of the frequency corresponding to the droplet spacing was measured from when TPX2 initially coated the microtubule to after the droplets had formed, for many microtubules. The power was then plotted over time.

Reporting Summary. Further information on research design is available in the Nature Research Reporting Summary linked to this article.

Data availability

Source data are provided with this paper. All other data that support the plots within this paper and other findings of this study are available from the corresponding author upon reasonable request.

Code availability

Algorithms and simulation codes are described in Methods and Supplementary Information.

References

36. Alfaro-Aco, R., Thawani, A. & Petry, S. Structural analysis of the role of TPX2 in branching microtubule nucleation. *J. Cell Biol.* **216**, 983–997 (2017).
37. Song, J. et al. Mechanism of how augmin directly targets the γ-tubulin ring complex to microtubules. *J. Cell Biol.* **217**, 2417–2428 (2018).
38. Murray, A. W. & Kirschner, M. W. Cyclin synthesis drives the early embryonic cell cycle. *Nature* **339**, 275–280 (1989).
39. Hannak, E. & Heald, R. Investigating mitotic spindle assembly and function in vitro using *Xenopus laevis* egg extracts. *Nat. Protoc.* **1**, 2305–2314 (2006).
40. Case, R. B., Pierce, D. W., Hom-Booher, N., Hart, C. L. & Vale, R. D. The directional preference of kinesin motors is specified by an element outside of the motor catalytic domain. *Cell* **90**, 959–966 (1997).
41. Gell, C. et al. in *Methods in Cell Biology* Vol. 95 (eds Wilson, L. & Correia, J. J.) 221–245 (Elsevier, 2010).
42. Schindelin, J. et al. Fiji: an open-source platform for biological-image analysis. *Nat. Methods* **9**, 676–682 (2012).
43. Hamon, L., Curmi, P. A. & Pastré, D. in *Methods in Cell Biology* Vol. 95 (eds Wilson, L. & Correia, J. J.) 157–174 (Elsevier, 2010).
44. Nečas, D. & Klapetek, P. Gwyddion: an open-source software for SPM data analysis. *Open Phys.* **10**, 181–188 (2012).
45. Thevenaz, P., Ruttimann, U. E. & Unser, M. A pyramid approach to subpixel registration based on intensity. *IEEE Trans. Image Process.* **7**, 27–41 (1998).

Acknowledgements

We thank S. Lee, T.-M. Chou and M. Libera at Stevens Institute of Technology for access to their atomic force microscope; I. Armstrong and S. Dutta at Bruker for access to and support for their atomic force microscope; M. King, B. Bratton, M. Safari, M. Koch, P. Ronceray and N. Wingreen for discussions; A. Thawani for purification of TPX2; H. Ando, C. Holmes, physiology students V. Baena, D. Laundon and L. Ma, and the Physiology Course at the Marine Biological Lab for assisting with the first AFM trials; and Princeton's Imaging and Analysis Center, which is partially supported by the Princeton Center for Complex Materials, an NSF-MRSEC programme (DMR-1420541). B.G. was supported by PD Soros and NSF GRFP. S.U.S. was supported by NIH NCI NRSA 1F31CA236160 and NHGRI training grant 5T32HG003284. This work was funded by NIH NIA 1DP2GM123493, Pew Scholars Program 00027340, Packard Foundation 2014-40376 and CPBF NSF PHY-1734030.

Author contributions

S.U.S., B.G., J.W.S., H.A.S. and S.P. conceptualized the project. B.G. and S.U.S. performed fluorescence microscopy, and B.G. performed analysis of fluorescence microscopy data. B.G. performed TPX2-only electron microscopy with assistance from R.A.-A. and S.U.S., theory and simulations. S.U.S. and B.G. performed AFM, and S.U.S. performed analysis of AFM data. S.U.S. performed meiotic cytosol experiments. R.A.-A. performed branching reconstitution and multiple-protein electron microscopy, and S.U.S. performed analysis of branching reconstitution data. S.U.S. and B.G. wrote the paper with assistance from J.W.S., H.A.S. and S.P. J.W.S., H.A.S. and S.P. supervised the research. All authors discussed and interpreted results and revised the paper.

Competing interests

The authors declare no competing interests.

Additional information

Extended data is available for this paper at https://doi.org/10.1038/s41567-020-01141-8.

Supplementary information is available for this paper at https://doi.org/10.1038/s41567-020-01141-8.

Correspondence and requests for materials should be addressed to J.W.S., H.A.S. or S.P.

Peer review information *Nature Physics* thanks Amy Gladfelter and the other, anonymous, reviewer(s) for their contribution to the peer review of this work.

Reprints and permissions information is available at www.nature.com/reprints.

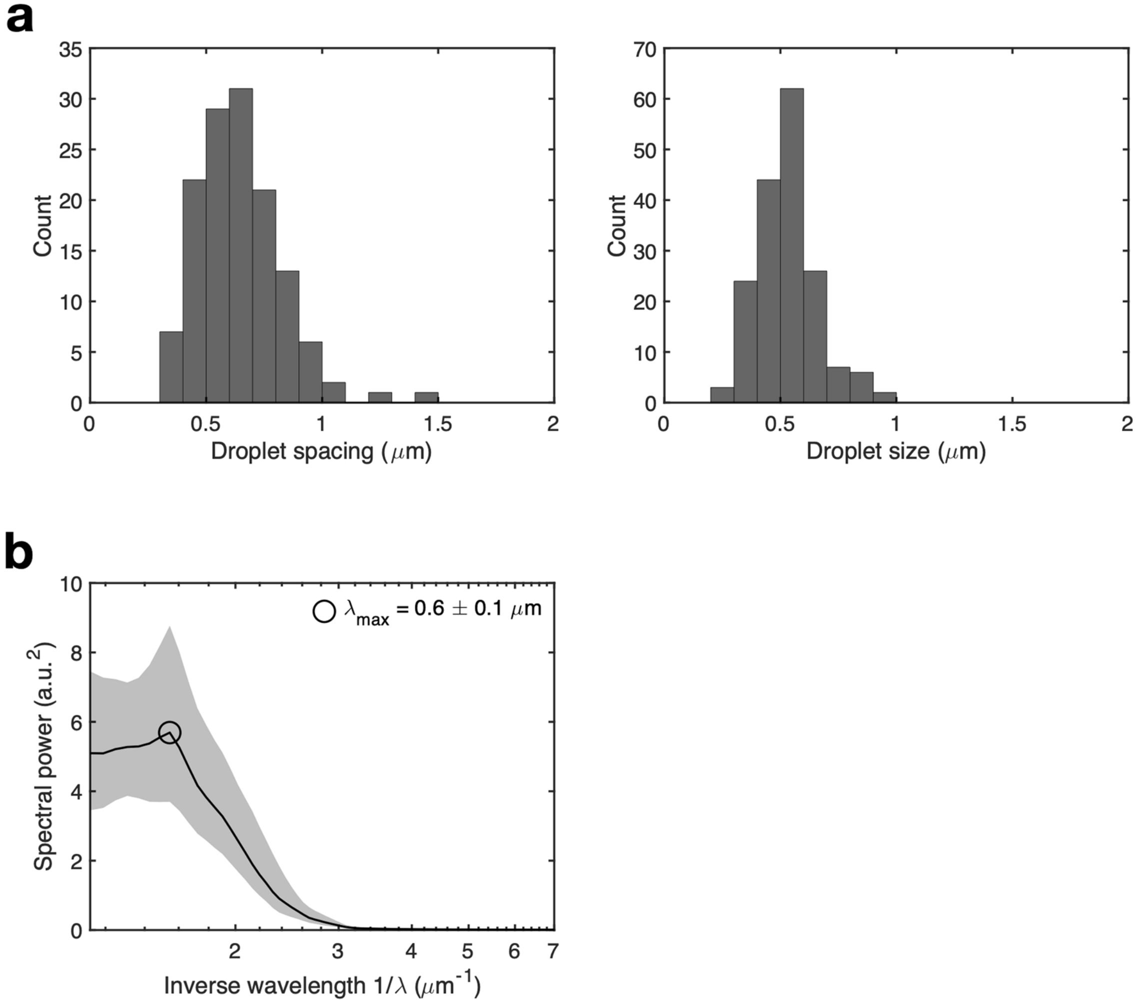

Extended Data Fig. 1 | Statistics of droplet patterned microtubules imaged with TIRF microscopy. a, Histogram of droplet sizes and spacings for TIRF experiments at 1 μM GFP-TPX2. $N = 35$ microtubules were analyzed with a mean size of $0.5 \pm 0.1 \mu$m and spacing $0.6 \pm 0.2 \mu$m (mean ± standard deviation). **b**, Average power spectrum of GFP-TPX2 fluorescence intensities of droplet patterns for TIRF experiments at 1 μM GFP-TPX2 ($N = 35$ microtubules). The peak indicates the emergence of a periodic pattern with wavelength $\lambda_{max} = 0.6 \pm 0.1 \mu$m (mean ± standard deviation), in agreement with the histogram analysis. Shaded regions are 95% bootstrap confidence intervals. For calculation details, see Methods.

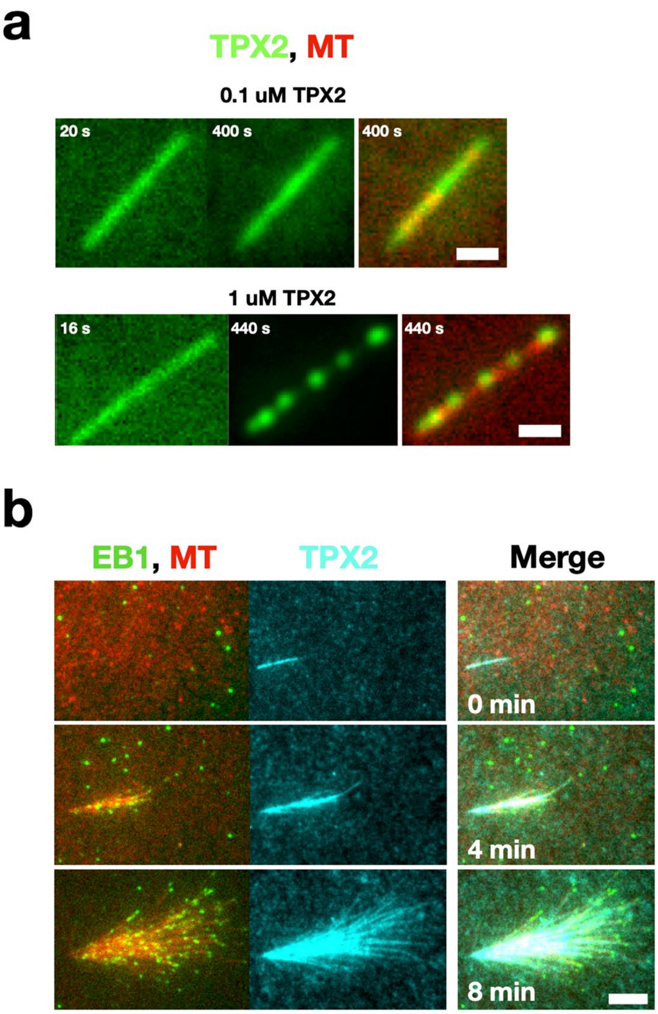

Extended Data Fig. 2 | TPX2 on the microtubule can appear uniform when imaged via optical microscopy. **a**, TIRF microscopy time lapses showing that a 0.1 μM TPX2 coating does not break up into visible droplets like the 1 μM TPX2 coating does. **b**, Branching microtubule nucleation visualized by TIRF microscopy in *X. laevis* meiotic cytosol at 0.1 μM TPX2, indicating that branching can occur from diffraction limited droplets.

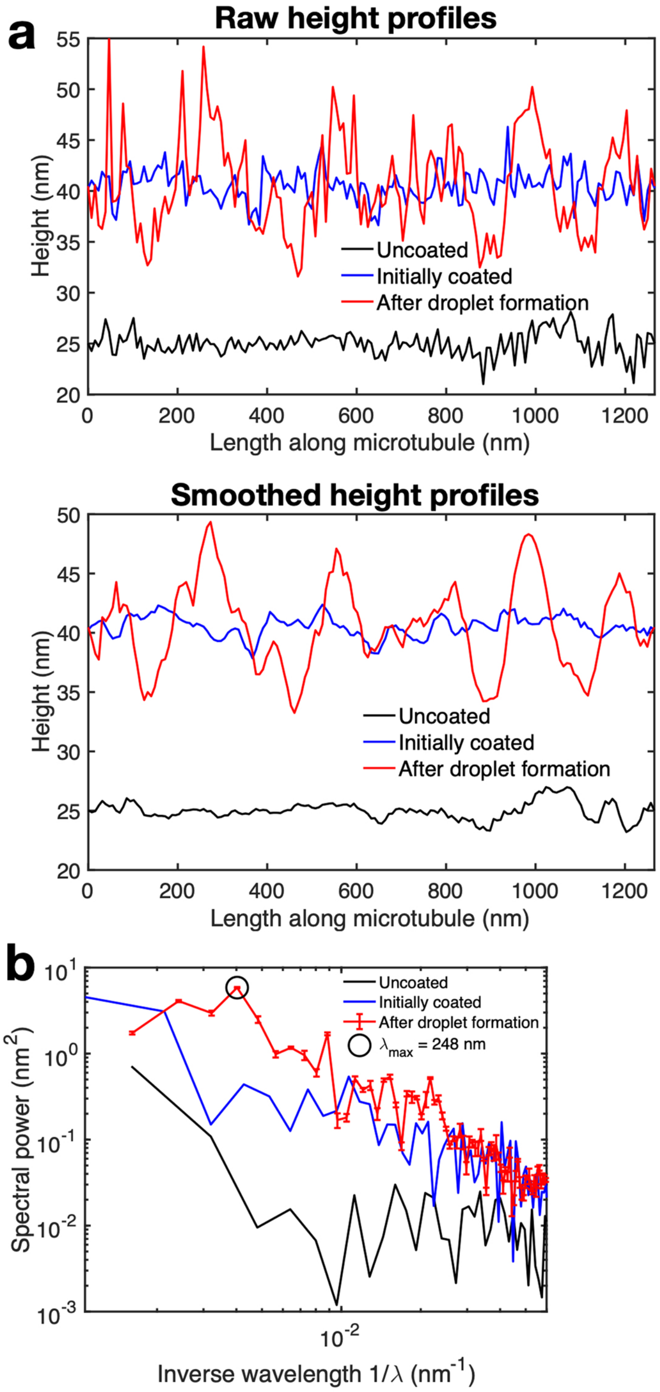

Extended Data Fig. 3 | Raw and smoothed AFM height profiles, and power spectra of raw height profiles. a, Raw height profiles of the topographies in Fig. 2a. The smoothed profile from Fig. 2b is shown again for reference. **b**, Power spectra of the raw height profiles in (**a**). The red curve shows the mean ± standard error of the mean over nine topographies of the microtubule after the droplet pattern had formed. The frequency *f* at which the peak in the red curve occurs gives the droplet spacing measured for this microtubule, according to $\lambda = 1/f$.

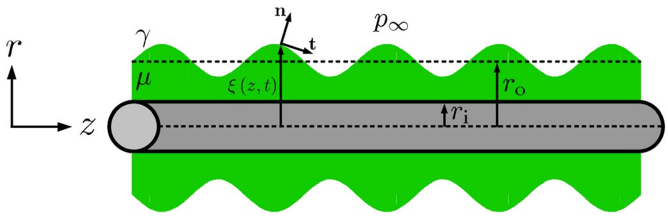

Extended Data Fig. 4 | Schematic of the Rayleigh-Plateau instability. The viscosity of the condensed film is μ, γ is the surface tension of the interface, and p_∞ is the far field pressure provided by the solvent. The microtubule has radius r_i. Initially, the interface is flat at $\xi(z, t = 0) = r_\mathrm{o}$, but this scenario is unstable against the capillary pressure γ/r_o, so $\xi(z, t)$ will evolve to a lower energy state. The unit normal **n** and unit tangent **t** track the geometry of the interface during its evolution.

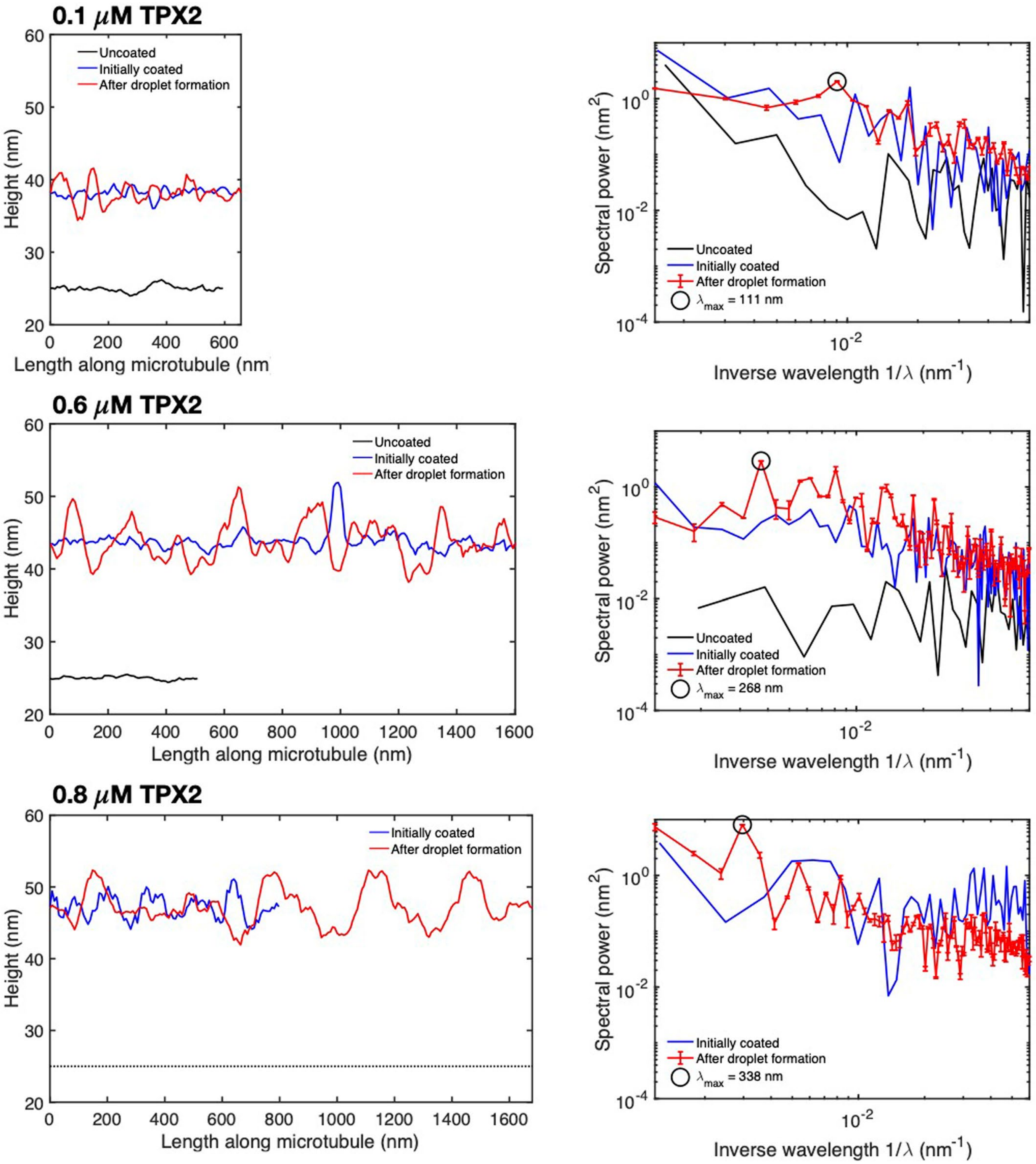

Extended Data Fig. 5 | AFM height profiles and power spectra at additional TPX2 concentrations. For 0.1 μM, the power spectrum is averaged over $N=5$ topographies after the droplet pattern had formed. For 0.6 μM, $N=3$. For 0.8 μM, $N=4$; the uncoated height profile for this specific microtubule is unavailable because the sample moved after TPX2 addition. Height profiles were smoothed using a moving-average window of 40nm. All power spectra after droplet formation show mean ± standard error of the mean.

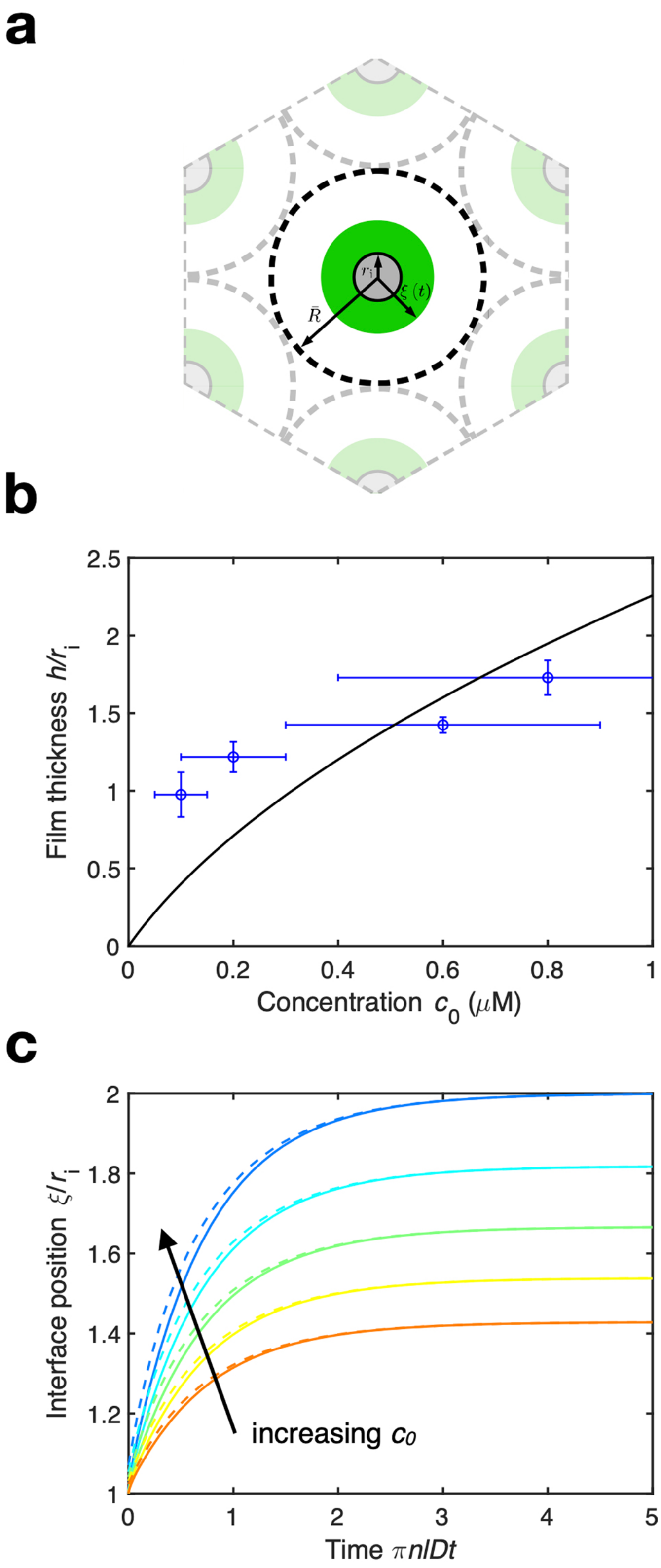

Extended Data Fig. 6 | Growth of the condensed film. a, Schematic of the model for growth of the condensed protein film. Microtubules of radius r_i are spaced periodically by a distance $2\bar{R}$, where $\bar{R} = 1/\sqrt{\pi nl}$ where l is the typical microtubule length and n is the number density of microtubules. Soluble protein phase separates from solution and nucleates a spatially uniform condensed film on the microtubule surface, whose interfacial position we denote by $r = \xi(t)$. **b**, Final film thickness h versus initial concentration c_0 as measured by atomic force microscopy (blue) and as predicted by equation (19) (black) and using $1/c_R\left(\bar{R}^2/r_i^2 - 1\right)$ as a least-squares fit parameter. **c**, Evolution of the interfacial position of the film ξ/r_i over time T for $S = r_i/r_o \in [0.5, 0.7]$, which is our experimentally observed range of S. Solid lines are the exact solution and dashed lines are the asymptotic formula (34b).

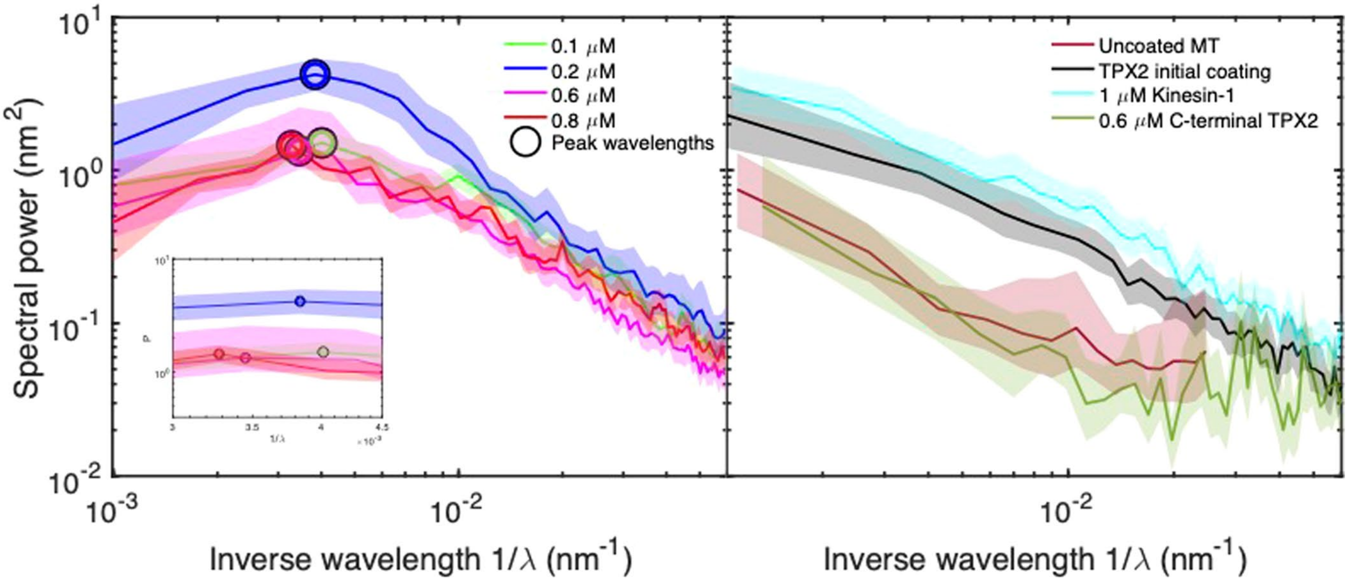

Extended Data Fig. 7 | Average power spectra from AFM data for all concentrations of TPX2 and for uncoated, initially TPX2-coated, C-terminal-TPX2-bound, and kinesin-1-bound microtubules. Peaks indicate characteristic wavelengths that correspond to a typical droplet spacing (Supplementary Table 3) (*N* = 25, 17, 23, and 21 microtubules, respectively, for increasing TPX2 concentration). Also included are average power spectra for uncoated microtubules (*N* = 29 microtubules), microtubules initially coated uniformly with TPX2 (*N* = 25 microtubules), kinesin-bound microtubules (*N* = 19 microtubules), and C-terminal-TPX2-bound microtubules (*N* = 4 microtubules)—none of which show any characteristic spatial features. For kinesin-bound microtubules, $h = 2.9 \pm 2.0$nm, consistent with what one would expect for the kinesin construct used[27,28]. For C-terminal-TPX2-bound microtubules, $h = 3.7 \pm 1.8$nm. Heights are mean ± standard deviation. Shaded regions represents 95% bootstrap confidence intervals.

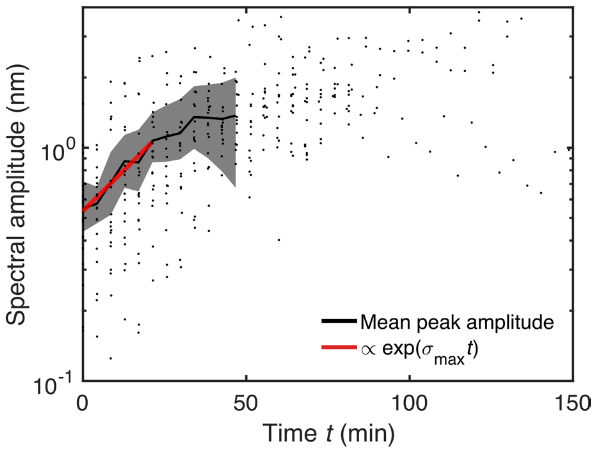

Extended Data Fig. 8 | The growth of the instability for early times is exponential. The average spectral amplitude at the most unstable frequency grows exponentially for early times (black line, $N = 21$ microtubules). Spectral amplitude $= \sqrt{\text{spectral power}}$. Individual measurements are black dots. Shaded region represents 95% bootstrap confidence intervals. At later times, the spectral amplitude levels off due to nonlinear forces as the pattern sets in. For the exponential fit (red), $\sigma_{\text{max}} = 0.03\,\text{min}^{-1}$, with $R^2 = 0.95$.

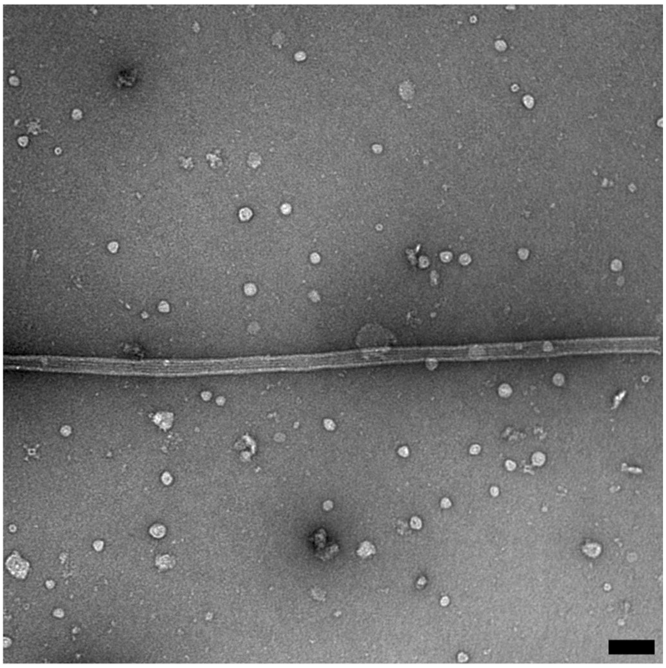

Extended Data Fig. 9 | γ-TuRC localization on bare microtubules. Typical electron microscopy experiment with just γ-TuRC and microtubules. Clearly, the localization of γ-TuRC to the microtubule without TPX2 and augmin is negligible (Supplementary Table 4). Scale bar is 100 nm.

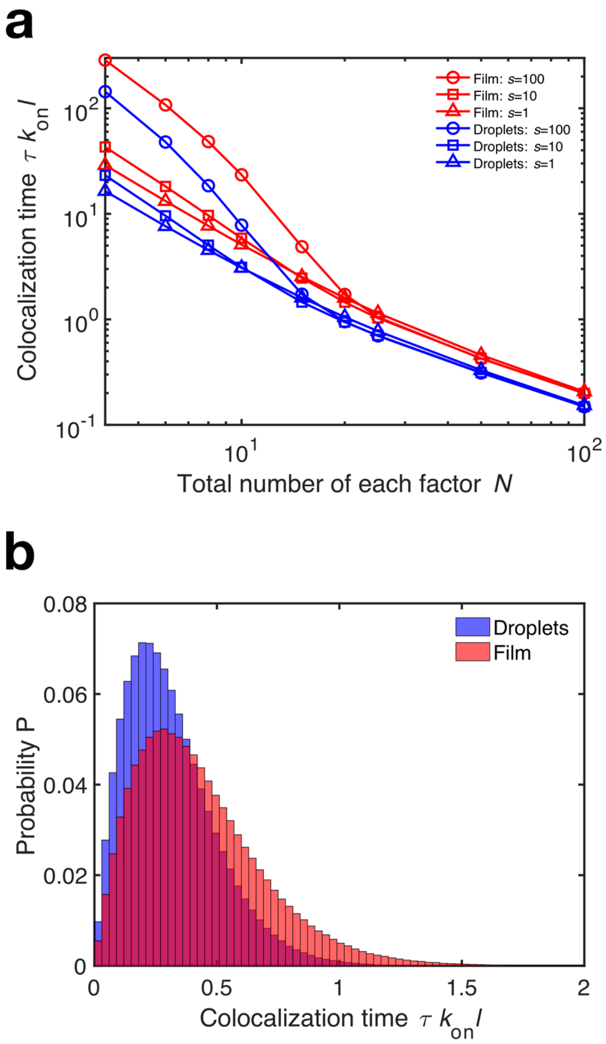

Extended Data Fig. 10 | Parametric study of Monte Carlo simulations. a, Time τ to colocalize two distinct factors, and hence form a branch, as a function of N and s for a uniform and periodic protein coating. For a given s, the periodic coating is uniformly more efficient at colocalizing well-mixed factors. Each data point is the average of 10^7 independent simulations. **b**, Typical histogram of 10^7 independent simulations for $F=2$, $N=50$, and $s=10$.

nature research

Corresponding author(s): Joshua W. Shaevitz, Howard A. Stone, Sabine Petry

Last updated by author(s): Feb 6, 2020

Reporting Summary

Nature Research wishes to improve the reproducibility of the work that we publish. This form provides structure for consistency and transparency in reporting. For further information on Nature Research policies, see Authors & Referees and the Editorial Policy Checklist.

Statistics

For all statistical analyses, confirm that the following items are present in the figure legend, table legend, main text, or Methods section.

n/a	Confirmed	
☐	☒	The exact sample size (*n*) for each experimental group/condition, given as a discrete number and unit of measurement
☐	☒	A statement on whether measurements were taken from distinct samples or whether the same sample was measured repeatedly
☐	☒	The statistical test(s) used AND whether they are one- or two-sided *Only common tests should be described solely by name; describe more complex techniques in the Methods section.*
☒	☐	A description of all covariates tested
☒	☐	A description of any assumptions or corrections, such as tests of normality and adjustment for multiple comparisons
☐	☒	A full description of the statistical parameters including central tendency (e.g. means) or other basic estimates (e.g. regression coefficient) AND variation (e.g. standard deviation) or associated estimates of uncertainty (e.g. confidence intervals)
☒	☐	For null hypothesis testing, the test statistic (e.g. *F*, *t*, *r*) with confidence intervals, effect sizes, degrees of freedom and *P* value noted *Give P values as exact values whenever suitable.*
☒	☐	For Bayesian analysis, information on the choice of priors and Markov chain Monte Carlo settings
☒	☐	For hierarchical and complex designs, identification of the appropriate level for tests and full reporting of outcomes
☒	☐	Estimates of effect sizes (e.g. Cohen's *d*, Pearson's *r*), indicating how they were calculated

Our web collection on statistics for biologists contains articles on many of the points above.

Software and code

Policy information about availability of computer code

Data collection	Atomic force microscopy: Bruker NanoScope 9.4, Fluorescence microscopy: NIS Elements 4.5, Electron microscopy: Advanced microscopy techniques, Stochastic simulations: custom Python3 script.
Data analysis	Atomic force microscopy: Gwyddion 2.53, ImageJ (FIJI) 2.0.0-rc-69/1.52p, custom MATLAB_R2017b script. Fluorescence microscopy: ImageJ (FIJI) 2.0.0-rc-69/1.52p, Electron microscopy: ImageJ (FIJI) 2.0.0-rc-69/1.52p, Stochastic simulations: custom Python3 script.

For manuscripts utilizing custom algorithms or software that are central to the research but not yet described in published literature, software must be made available to editors/reviewers. We strongly encourage code deposition in a community repository (e.g. GitHub). See the Nature Research guidelines for submitting code & software for further information.

Data

Policy information about availability of data

All manuscripts must include a data availability statement. This statement should provide the following information, where applicable:

- Accession codes, unique identifiers, or web links for publicly available datasets
- A list of figures that have associated raw data
- A description of any restrictions on data availability

All data will be made available upon request.

Field-specific reporting

Please select the one below that is the best fit for your research. If you are not sure, read the appropriate sections before making your selection.

☒ Life sciences ☐ Behavioural & social sciences ☐ Ecological, evolutionary & environmental sciences

For a reference copy of the document with all sections, see nature.com/documents/nr-reporting-summary-flat.pdf

Life sciences study design

All studies must disclose on these points even when the disclosure is negative.

Sample size	Individual microtubules were counted.
Data exclusions	None.
Replication	Multiple independent samples were prepared and measured. Multiple methods of data acquisition were used (atomic force, fluorescence, and electron microscopies). All attempts at replication were successful.
Randomization	Not applicable.
Blinding	Not applicable.

Reporting for specific materials, systems and methods

We require information from authors about some types of materials, experimental systems and methods used in many studies. Here, indicate whether each material, system or method listed is relevant to your study. If you are not sure if a list item applies to your research, read the appropriate section before selecting a response.

Materials & experimental systems

n/a	Involved in the study	
☐	☒	Antibodies
☒	☐	Eukaryotic cell lines
☒	☐	Palaeontology
☐	☒	Animals and other organisms
☒	☐	Human research participants
☒	☐	Clinical data

Methods

n/a	Involved in the study	
☒	☐	ChIP-seq
☒	☐	Flow cytometry
☒	☐	MRI-based neuroimaging

Antibodies

Antibodies used	anti-Biotin (Abcam, ab1227, polyclonal), anti-gamma-tubulin (Sigma, T6557-.2ML, clone GTU88), anti-TPX2 (GenScript, custom raised in rabbits against recombinant TPX2, polyclonal), anti-rabbit-IgG (Sigma, I5006, polyclonal).
Validation	For immunodepletion from Xenopus laevis meiotic cytosol, TPX2 and rabbit IgG antibodies were confirmed to be specific via western blot and silver staining. For purifying g-TuRC, purity of final product was determined by electron microscopy. For biotin antibody, biotinylated microtubules were visualized to be attached to the antibody-coated coverslip via fluorescence microscopy.

Animals and other organisms

Policy information about studies involving animals; ARRIVE guidelines recommended for reporting animal research

Laboratory animals	Species: Xenopus laevis, sex: female, age: mature.
Wild animals	None.
Field-collected samples	None.
Ethics oversight	All animals were cared for according to the approved Institutional Animal Care and Use Committee (IACUC) protocol 1941-16 of Princeton University.

Note that full information on the approval of the study protocol must also be provided in the manuscript.